Aerospace Science and Technology 82–83 (2018) 294–303

Contents lists available at ScienceDirect

Aerospace Science and Technology

www.elsevier.com/locate/aescte

Experimental study on the accretion and release of ice in aviation jet fuel

Mathias Schmitz *, Gerhard Schmitz

Hamburg University of Technology, Institute of Engineering Thermodynamics, Denickestr. 15, 21073 Hamburg, Germany

ARTICLE INFO

Article history:
Received 10 May 2018
Received in revised form 25 August 2018
Accepted 27 August 2018
Available online 7 September 2018

Keywords:
Fuel system
Aviation fuel
Low temperatures
Water
Ice accretion
Ice formation

ABSTRACT

Ice formations in aircraft fuel systems pose a serious safety threat with potentially disastrous consequences, when restricting the fuel flow towards the engines. This is an ongoing challenge in the aerospace industry. In this work experimental studies have been performed to investigate the effects of temperature, flow rate and surface properties on the accretion and release of ice in flowing fuel. A test rig with a glass-windowed pipe has been employed to quantitatively measure the transient icing process under controlled conditions. The accreted ice exhibited soft and fluffy characteristics and was most likely the result of impinging solid ice particles that were entrained in the fuel flow. The ice particles were most sticky in a temperature range between −6°C and −20°C. The thickness of accreted ice decreased with roughness on aluminium surfaces and there was a significant reduction on polytetrafluoroethylene (PTFE) and polymethyl methacrylate (PMMA) in comparison to aluminium, copper or stainless steel surfaces. Comparison of the thickness of accreted ice with the ice adhesion strength reported in the literature showed a clear correlation. The experimental results will help to gain better understanding of the ice accretion process in flowing fuel and may serve as basis for design guidelines to minimize ice formation within an aircraft fuel system.

1. Introduction

Aviation fuels are known to contain small quantities of dissolved water. The solubility decreases with temperature and any excess water is precipitated out when the fuel is cooled [1–3]. As jet aircraft are exposed to very low temperatures, the water may lead to ice formations within the fuel system with possible detrimental effect upon the fuel flow. Numerous corrective measures were developed to prevent this, which include the use of anti-icing fuel additives, fuel heaters, improved temperature monitoring [4] and bypasses around mesh strainers [5]. These measures effectively address the problem, but do not necessarily address the root cause [5]. After the investigation of the Boeing 777 crash landing at Heathrow airport in January 2008, the Air Accident Investigation Branch (AAIB) expressed concerns about the lack of understanding of the nature and behaviour of water in jet fuel and made recommendations for further research [6,5].

Murray et al. [7] investigated the freezing behaviour of micron sized water droplets immersed in Jet A-1 aviation fuel. They found that the majority of these droplets were able to remain in a metastable supercooled state till around −36°C. Lam et al. made similar observations for some water droplets that precipitated out from a model fuel (toluene) below −30°C [8].

Lao et al. [9] studied the transition from dissolved water to the deposition of ice on subcooled surfaces using a simulated fuel tank. They observed a fairly uniform thin layer of spherical droplets/particles that formed on top of an aluminium block. The deposition seemed to grow directly from the dissolved phase. They compared the growth characteristics with the initial frost formation period described in [10] and suggested that the ice deposition was due to the Bergeron process. Similarly, Lam et al. [8] observed a mass transfer from metastable (spherical) ice particles to hexagonal ice particles and attributed this to the augmented Wegener–Bergeron–Findeisen process and the Ostwald ripening process.

Lam et al. [11] described the ice that accreted on subcooled surfaces as soft and fluffy, much akin to fresh snow. The ice possessed a very high porosity and little adhesion strength.

After the incident at Heathrow in 2008, Boeing's Kent Fuels Laboratory and the North Boeing Field Propulsion Laboratory conducted experiments on ice accretion within fuel lines using a mock-up of the aircraft's fuel delivery system [6]. Their results suggested a "sticky" region between temperatures ranging from −5°C and −20°C, in which ice particles tend to adhere to surfaces and to each other. In [12,4] such sticky behaviour is described between

* Corresponding author.
E-mail address: mathias.schmitz@tuhh.de (M. Schmitz).

https://doi.org/10.1016/j.ast.2018.08.034

Nomenclature

Abbreviations

AAIB	Air Accident Investigation Branch
AL	aluminium
CU	copper
PMMA	polymethyl methacrylate
PTFE	polytetrafluoroethylene
SST	stainless steel

Latin symbols

A	area in m^2
d	diameter in m
$D_\mathbf{h}$	hydraulic diameter in m
h	height in m
l	length in m
$R_\mathbf{a}$	arithmetic average roughness in m
$t_\mathbf{a}$	ice thickness in m
$\overline{t}_\mathbf{a}$	average ice thickness in m
U	velocity in m/s
$\dot{V}$	volume flow in l/h
w	width in m

Greek symbols

γ	mass content in ppm_{mass}
ϑ	temperature in °C
Θ	temperature in K
$\overline{\Lambda}_\mathbf{a}$	normalized maximum average ice thickness
τ	time in s
$\overline{\Omega}$	ice release ratio

Subscripts

a	accretion of ice
b	bulk
C	test body centre piece
CH	chiller
D	duct
H	test body holder
r	release
ref	reference
s	steady state, solubility
t	target (temperature or volume flow rate), total (water content)
TS	test section
u	undissolved (water content)
w	water
○	target temperature reached
□	start volume flow increase
△	end volume flow increase
◊	start temperature increase

temperatures of −12°C and −18°C. Murray et al. [7] suggested that the sticky ice particles are in fact supercooled water droplets that freeze heterogeneously when coming into contact with a solid surface.

The accreted ice found in the AAIB tests was soft and mobile [6]. Considerable amounts could be shed off the inner pipe surfaces by increasing the flow rate. The ice shedding resulted in a high particle concentration that was able to clog a fuel-oil heat exchanger and hence restrict the fuel flow. The sudden release of accreted ice is often referred to as “snow shower” [11,13].

In summary, the icing of aircraft fuel systems is affected by a complex interaction of water precipitated, mass transfer, phase change, accretion onto surfaces as well as the subsequent release. Although enhanced efforts have been devoted to the research recently, the underlying mechanisms are still poorly understood. The main objective of this study is to gain further understanding of the transient ice accretion and release process in flowing fuel and of the effect of the temperature, flow rate, surface roughness and surface material.

2. Materials and methods

2.1. Test rig

Fig. 1 shows a schematic of the test rig employed for this study. The fuel flow is fed from a welded aluminium tank of 100 l capacity and driven by a gear pump (Typ KF-F 16 RF 2-ATEX, Kracht, Germany). The pump speed is controlled by a PID controller implemented in the central data acquisition and control system (LabVIEW). A plate type heat exchanger is used to cool the circulating fuel. The required cooling capacity is provided by a chilling system (Integral Process Thermostats T10000, Lauda, Germany) which is connected to the fuel system through a secondary cooling loop with a monoethylene glycol-water mixture.

Key component of the apparatus is the test section. Here, the fuel passes through a straight rectangular duct ($l_D = 840$ mm in length, $w_D = 15.8$ mm in width, $h_D = 18.0$ mm in height). The two opposing sidewalls are made of triple-glazed insulating windows. This permits visual observation of the icing process within the cold fuel flow as well as the application of non-intrusive optical measurement techniques. In order to avoid any view blocking ice accretion on the glass windows, the inner (fuel wetted) sides are covered with a thin layer of acrylic glass (polymethyl methacrylate, PMMA), which, in preliminary studies, was found to have limited affinity to ice.

After traversing the test section, the fuel flows back into the tank. The test rig piping consists of stainless steel pipes having an inside diameter of 19.6 mm. The entire test rig is thermally insulated with 38 mm Armaflex/AF (Armacell, Luxembourg).

The test rig is instrumented with a total number of 19 type T thermocouples. They are located, for instance, at the inlet and outlet of the test section, in the tank, after the heat exchanger and after the pump. A Coriolis flow meter (FC Massflo Mass 2100, Siemens, Germany) is used to measure the volume flow rate. The total water content of the fuel is determined by Karl Fischer titration (TitroLine 7500 KF trace, SI Analytics, USA) using the sampling bypass as shown in Fig. 1.

The test rig is designed to operate at a minimum fuel temperature of −22°C and a maximum volume flow rate of 1200 l/h. According to the fuel properties given in [1], this corresponds to a bulk velocity in the test section of $U_{b,TS} = 1.172$ m/s and a Reynolds number of $Re_{TS} = 4665$, the latter is based on the bulk velocity and the hydraulic diameter $D_{h,TS} = \frac{2 w_D h_D}{w_D + h_D} = 16.83$ mm.

2.2. Test bodies

In this work, the ice accretion is studied using exchangeable test bodies. These test bodies are mounted transversely to the direction of flow between the transparent side walls of the test section, see Fig. 2. The test bodies create a deflection of the oncoming fuel flow and therefore promote the deposition of entrained ice particles. In real aircraft fuel systems, such significant flow deflections can be found, for example, in sharp pipe bends, connectors, valves, pump inlet screens or feed ejector pump orifices.

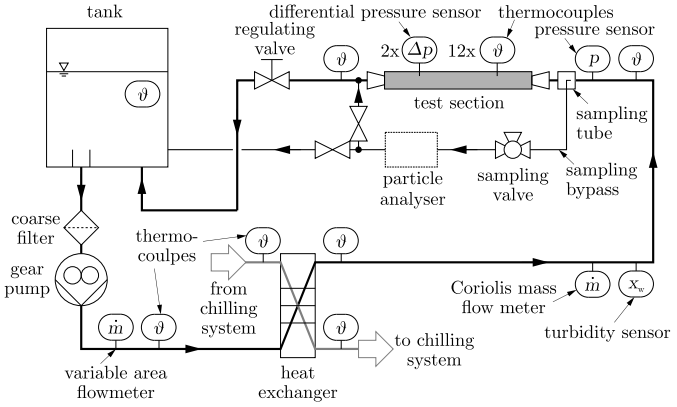

Fig. 1. Simplified schematic of the icing test rig.

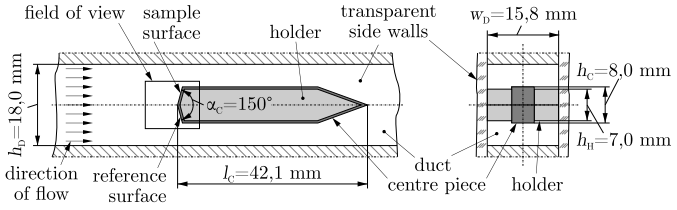

Fig. 2. Geometry and arrangement of the wedge shaped test body within the test section.

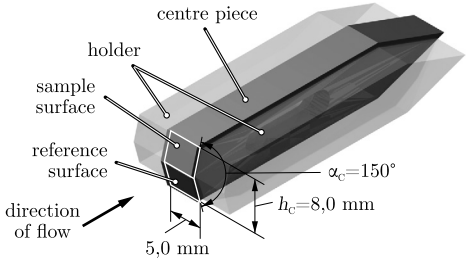

Fig. 3. Sketch of the wedge shaped test body used in this study, ■: centre piece, ■: holder.

The test bodies are an assembly of three parts: a centre piece and two holders, see Fig. 3. While the centre piece is the actual object against which the ice is supposed to accrete, the holders are required to keep the centre piece in position, however, without obstructing the side view towards the centre piece. They therefore have a slightly smaller cross-section and, in order to avoid any view blocking ice accretions, they are made of acrylic glass such as the duct's sidewalls. The test body assemblies are placed at the duct's centre line about 550 mm after the test section entrance. This corresponds to 33 times the hydraulic diameter.

Two sets of blunt, wedge shaped test bodies are prepared, as shown in Fig. 3. The first set is used to study the effect of surface roughness. For this, the surface of four aluminium centre pieces are altered mechanically: by polishing to a mirror finish (POL), by glass bead blasting (GBB) and by abrading with coarse (A400) or with fine (A3000) abrasive paper. As illustrated in Fig. 3, these different treatments are only applied to the upper half of each wedge, i.e. to the "sample surface", whereas the lower half of all wedges are treated by glass bead blasting (GBB). The latter serves as a "reference surface". Simultaneous observation of both halves allows a direct, comparative evaluation of icing behaviour.

The second set of wedges is prepared with the aim to study the effect of surface material. The centre pieces of five wedges are made out of: aluminium (AL), copper (CU), stainless steel (SST), polymethyl methacrylate (PMMA) and polytetrafluoroethylene (PTFE). To create similar and hence comparable surface topographies, all of the sample surfaces are polished.

All surfaces are characterised both, quantitatively in terms of surface roughness measured by a contact profilometer (XR20/GD120, Mahr, Germany) as well as qualitatively by microscopic images taken with Infinite Focus G4 (Alicona, Austria).

2.3. Ice accretion measurement

Quantitative measurement of the ice accretion process is performed by an imaging system in combination with digital image processing techniques. The imaging system comprises a 4608 pix × 3288 pix CMOS camera (acA4600-uc10, Basler, Germany) and a telecentric lens (CCTV LM1125TC, Kowa, Japan). The camera is aligned perpendicular to the test body in order to obtain a two dimensional projected view of the lateral extents of test body (including ice formations), as illustrated in Fig. 2. Only the frontal part of the wedge shaped test bodies is captured. The field of view is 14.798 mm × 10.559 mm, which corresponds to a pixel resolution of 3.211 µm/pix. A uniform background illumination is provided by a custom made led panel. The images are calibrated by the known dimensions of the test bodies.

A chain of digital image processing techniques are applied to automatically determine the ice accretion from the raw images. This involves two major steps: segmentation and gauging. By segmentation the object of interest, in this case the ice, is separated from the background, which is basically done by subtracting the currently investigated image from a reference image. The reference image is typically the first image of an experiment showing the naked test body. In this way, changes from the initial state, which must be due to the presence of ice, become visible. In the difference image the pixels are categorized as "ice" or "no ice" by applying a fixed threshold grayscale value. It has to be noted, however, that this method of segmentation would produce significant errors if there are even small misalignments between the investigated and the reference image. Such misalignments may be caused by displacements between the camera and the test body during the experiment, for instance due to thermal expansions or fluid dynamic pressures. As a countermeasure, misalignments are detected

prior to subtraction by an intensity-based image optimisation function and, if necessary, compensated by a corrective digital image shift.

After segmentation the ice is quantified in terms of a total cross-sectional area of ice, A_a, simply by counting the pixel representing ice. Furthermore, the ice is quantified in terms of a circumferential ice thickness t_a. For this, the (iced) test body contour is traced by a Moore–Neighbor tracing algorithm and, after transformation into a local coordinate system, subtracted from the contour of the naked test body.

For some experiments the CMOS camera is also equipped with a long-distance microscope (K2DistaMax, Infinity, USA) in order to capture detailed features of the ice formations.

2.4. Ice particles size and morphology analysis

A particle size and shape analyser (EyeTech, Ankersmid, Netherlands) is (temporally) installed within the fuel sampling bypass in order to visualise and measure the entrained water/ice particles (cf. Fig. 1). The particle analyser captures 345.6 µm × 259.2 µm (0.540 µm/pix) microscopic images of the fuel stream while passing through a cuvette. A stream of nitrogen is blown across the external surfaces of the cuvette to prevent condensation from forming at the low operation temperatures. Particle segmentation and gauging procedures are performed in post processing using the ImageJ distribution Fiji [14].

2.5. Experimental procedure

The tank is filled with about 60 l of Jet A-1, produced by a major UK oil refiner. For this study two different fillings (I & II) are used. For each filling, the fluid dynamic properties, namely density and viscosity, were measured by the Coriolis flow meter installed in the test rig (FC Massflo Mass 2100, Siemens, Germany) and an Ubbelohde viscometer (50101-0a, SI Analytics, USA), respectively. The water solubility was determined by Karl Fischer titration (TitroLine 7500 KF trace, SI Analytics, USA) in a similar procedure as described in [2].

The icing experiments are carried out with the fuel as received. No additional water is injected before or during the experiments, which means that any formations of ice arise solely from water that occurs naturally in the fuel, i.e. from water that is precipitated out during cooling. Injection of additional water as in [6,15,11,16,13] would increase the yield of ice accretion and hence enhance visualisation, but numerous additional factors and uncertainties related to such an injection (method, location, time) would artificially be introduced, which might deteriorate reproducibility.

The test bodies are cleaned with isopropyl alcohol and blown dry prior to installation.

A temperature and volume flow rate profile, as shown in Fig. 4, is used for the experiments. Starting from a chiller temperature of $\vartheta_{CH} = 20°C$ the fuel circulates for at least ten minutes in order to homogenise the fuel and to reach steady state condition. Afterwards, the fuel is cooled at a rate of $^{\Delta\vartheta_{CH}}/_{\Delta t} = 0.5°C/min$ until the desired target temperature $\vartheta_{CH,t}$ is reached. This temperature is maintained for at least 3 h and then, in order to evaluate the strength of the accreted ice, the volume flow rate is gradually increased at a rate of $^{\Delta\dot{V}}/_{\Delta t} = 20$ l/h/min ($^{\Delta U_{b,TS}}/_{\Delta t} = 0.0195$ m/s/min) up to $\dot{V} = 1000$ l/h ($U_{b,TS} = 0.977$ m/s). After five minutes, the volume flow rate is reduced to its previous value and another ten minutes later the heating starts with a rate 1.0°C/min. A slightly higher final temperature of 25°C is chosen to further raise the water solubility and hence accelerate the reabsorption of precipitated water. Between two experiments a reabsorption time of at least twelve hours is provided.

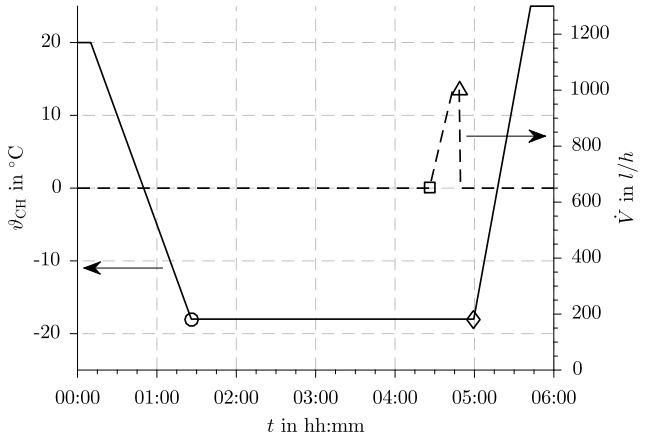

Fig. 4. Temperature and volume flow rate profile used in the experiments, shown here for $\vartheta_{CH,t} = -18°C$ and $\dot{V}_t = 650$ l/h. —: chiller temperature, – –: volume flow rate, ○: target temperature reached, □/ △: start/end volume flow rate increase, ◇: start temperature increase.

The effects of three parameters on the accretion and release of ice are studied. The test conditions are summarized in Table 1. The fuel filling is not changed when investigating a parameter effect. At least three experiments are carried out for each condition.

The evaluation of ice accretion is primarily based on the maximum average ice thickness that is obtained on the upstream side of a test body during an experiment (between ○ and □ in Fig. 4):

$$\bar{t}_{a,max} = \max\left(\bar{t}_{a,\bigcirc\ldots\square}\right) \tag{1}$$

Furthermore, the normalized release of ice caused by the increasing volume flow rate (between □ and △ in Fig. 4) is used as a measure for the ice strength:

$$\overline{\Omega}_a = \frac{\Delta_{release}\bar{t}_a}{\bar{t}_{a,\square}} = \frac{\bar{t}_{a,\square} - \bar{t}_{a,\triangle}}{\bar{t}_{a,\square}} \tag{2}$$

The hydraulic diameter of the rectangular test section ($D_{h,TS} = 16.83$ mm $\approx 0.66''$) is within the range of pipe diameters that are typically used in an aircraft's fuel delivery system ($\approx 0.5''$–$2.5''$).

The flow and temperature conditions are quite moderate. They are believed to be of particular relevance. The investigated temperatures are within the sticky ice region and the moderate flow rates are expected to yield significant ice formations as accreted ice seems to be soft and mobile [6] with very little adhesion strength [9,11].

The overall fuel cooling rate in this work is of the same order of magnitude as that in a real aircraft fuel tank during typical missions [17,15]. Within the heat exchanger, the skin temperature can be significantly lower than that of the inflowing fuel.[1] Due to this, the fuel may experience a comparatively rapid cooling of up to $\Delta\vartheta = 5.3°C$ (220 l/h) and $\Delta\vartheta = 2.3°C$ (650 l/h) while passing through the heat exchanger. This might apply a thermal shock to part of the fuel. During the investigations, however, there were no indications for a possible effect on the general ice accretion behaviour presented hereafter, e.g. when there was a change in the volume flow or the cooling rate.

[1] The temperature difference between the inflowing fuel and the heat exchanger plates is estimated from the fuel temperature in the tank and the temperature of the cooling fluid when entering the heat exchanger. The maximum difference appears at the end of the cooling phase (indicated by ○ in Fig. 4) and can as much as $\Delta\vartheta = 6.9°C$ for 220 l/h and $\Delta\vartheta = 3.1°C$ for 650 l/h.

Table 1
Test conditions.

No	influence of...	$\vartheta_{CH,t}$ in °C	$\dot{V}_t$ in l/h	test bodies	fuel filling
1	temperature on ice accretion	−22–−6	650[2]	wedge shaped	I
2	surface roughness on ice accretion & release	−18	220[1] & 650[2]	wedge shaped, set 1	II
3	material on ice accretion & release	−18	220[1] & 650[2]	wedge shaped, set 2	II

[1] $\dot{V}_t = 220$ l/h $\equiv U_{b,TS} = .215$ m/s $\equiv Re_{TS} = 1014$ at $\vartheta_{TS,s} = -17.3$°C.
[2] $\dot{V}_t = 650$ l/h $\equiv U_{b,TS} = 0.635$ m/s $\equiv Re_{TS} = 2996$ at $\vartheta_{TS,s} = -17.3$°C.

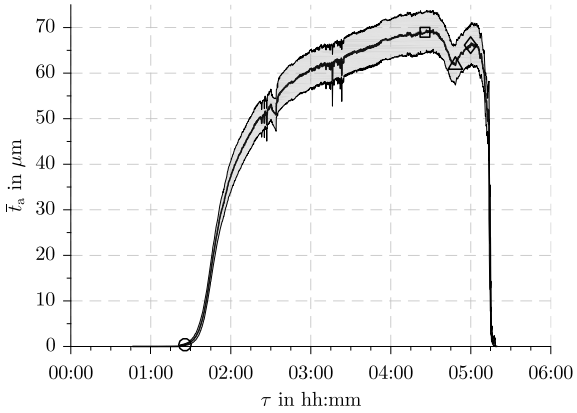

Fig. 5. Growth of ice on aluminium with glass bead blasted (GBB) surface finish. Average ice thickness $\bar{t}_a$ for $\vartheta_{TS,s} = -17.3$°C and $\dot{V}_t = 650$ l/h. ○: target temperature reached, □/△: start/end volume flow rate increase, ◇: start temperature increase.

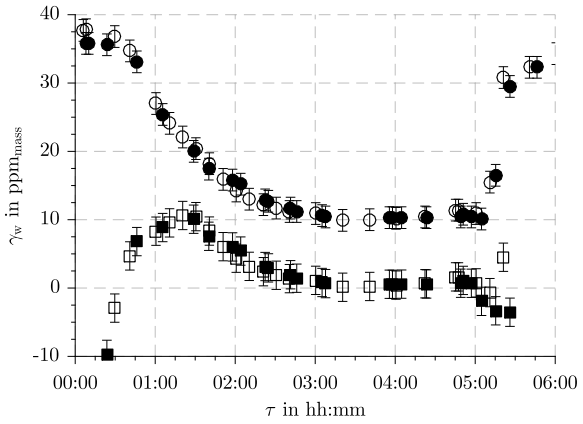

Fig. 6. Water content in Jet A-1 γ_w for $\vartheta_{TS,s} = -17.3$°C and $\dot{V}_t = 650$ l/h. ○/●: total water content $\gamma_{w,t}$, □/■: theoretical undissolved water content $\gamma_{w,u}$ (filled/not filled: first/last experiment of this series of experiments).

3. Results and discussion

3.1. Description of ice accretion process

The typical ice accretion process is illustrated for a reference experiment. Here, a test body is exposed to a fuel flow of 650 l/h ($U_{b,TS} = 0.635$ m/s). The chiller target temperature is set to $\vartheta_{CH,t} = -18$°C, which results in a slightly higher steady state fuel temperature in the test section of $\vartheta_{TS,s} = -17.3$°C. The Reynolds number is $Re_{TS} = 2996$. The reference experiment was carried out several times before and after the actual experiments presented hereafter in order to assure reproducibility. Unless stated otherwise, the following results are the average of eight individual runs. Error bars and patches are used to indicate the standard uncertainty, e.g. the experimental standard deviation of the mean [18].

In Fig. 5 the average ice thickness $\bar{t}_a$ on the upstream side of test body is plotted against time. Fig. 6 shows the total water content $\gamma_{w,t}$ along with the corresponding theoretical undissolved water content $\gamma_{w,u}$. The latter was derived using the fuel temperature and the measured water solubility. The uncertainty is estimated from repeated measurements that were carried out multiple times during certain points in time, i.e. during the warming-up phase and shortly before the increase of the volume flow.

The observations made during the experiment are as follows:

00:30 Water begins to separate from the fuel as the temperature drops below 10°C. Micron sized, spherical droplets ranging from about 2 µm to 10 µm appear in the particle analyser.

00:50 As the temperature reaches 0°C the water droplets could – at least in principle – solidify into ice particles. Their actual state is, however, undetermined as there is no visual change in their appearance.

01:26 A few minutes after reaching the target temperature water droplets/ice particles start to adhere to each other. They turn into fluffy, snowflake-like ice particles up to 250 µm in size. At the same time, particles begin to adhere to the test body surface, as can be seen from $\bar{t}_a$ in Fig. 5. In general, the visual appearance of the accreted particles is very similar to those observed in the fuel flow. Their morphological features as well as their sometimes partly interrupted contact to the surface (cf. Fig. 7) is an important clue which suggests that these particles were already of solid nature when striking the surface. Fig. 7 illustrates the icing process in a series of images taken with the long range microscope. After deposition, the single particle in Fig. 7a is first compressed from its initially ≈70 µm to ≈50 µm (cf. Fig. 7c), presumably due to the fluid dynamic forces acting on the (iced) surface. With further impingement of smaller and larger particles, the particle progressively grows in size (cf. Fig. 7d to 7h) and eventually, in an ongoing process of deposition and deformation, a thin, irregular layer is formed. The accreted ice can best be described as soft, deformable and mobile. It seems to be similar to the ice described in [11,6].

02:30 Most of the available undissolved water is "consumed" due to deposition within the system. The ice thickness curve flattens and the free water content tends towards zero.

04:26 Now, as a result of the gradually increasing volume flow rate between 04:26 and 04:48 (indicated by □ and △) part of the accreted ice is shed off, i.e. the ice thickness decreases ($\overline{\Omega}_a = 0.103$).

04:59 The remaining ice is shed off while the fuel is heated up again, mostly between temperatures of −5–−2°C (≈05:15). This can be seen from the ice thickness and the water content.

Comparison of the water content measured at the beginning (○) and the end (●) of this series of experiments (cf. Fig. 6) reveals no significant changes. This means that even after four months and several runs with the same fuel filling (II), an almost identical water content was achieved each time. This is in agreement with the small deviations in the individual ice thickness curves, as indicated by the standard uncertainty. In general, the measurement of the ice accretion shows results with good reproducibility. They confirm

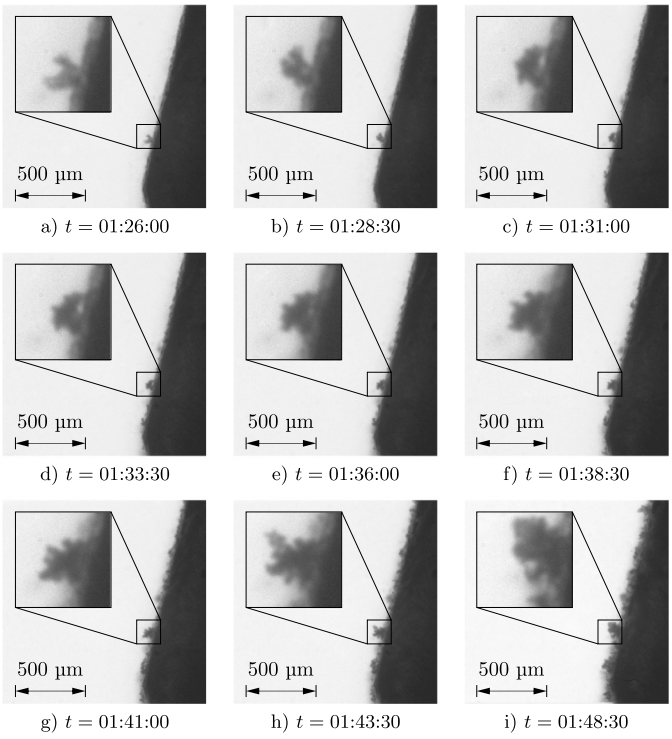

Fig. 7. Growth of ice on aluminium with glass bead blasted (GBB) surface finish. The microscopic images show the frontal part of the wedge shaped test body (cf. Fig. 3) at different points in time (cf. Fig. 4) for $\vartheta_{TS,s} = -17.3°C$ and $\dot{V}_t = 650$ l/h.

the suitability of the method applied in this work to systematically study the effect of various parameters.

3.2. Influence of temperature

Following the procedure described above, experiments were carried out at different target temperatures ranging from $\vartheta_{CH,t} = -6°C$ to $-22°C$. Fig. 8 shows the maximum average ice thicknesses obtained during the experiments, $\bar{t}_{a,max}$, as a function of the corresponding steady state fuel temperature in the test section $\vartheta_{TS,s}$. While no accretion of ice can be observed above $-6°C$, there is an almost linear relationship in a temperature range between $-6°C$ and $-15°C$. The increase in ice thickness can be partly attributed to a decreasing water solubility, because falling temperatures lead to a higher availability of undissolved water as more water comes out of solution. At test temperatures below $-15°C$ the ice thickness gradually levels off. The ice seems to lose its ability to adhere to the test body. In case of $\vartheta_{TS,s} = -20.8°C$, it was observed that large fractions of the initially accreted ice were subsequently shed off. This behaviour is well reflected in the fuel water content. Fig. 9 shows the remaining total water content at the end of the cooling period (□ in Fig. 4). A comparison with the water solubility (solid line) reveals a dramatic increase in the undissolved water content for temperatures below $-20°C$. This means, a much higher fraction of the precipitated water was not able to permanently settle or accrete within the system and thus still circulated with the fuel flow.

It seems unlikely that the deterioration in ice accretion arose from the moderate changes in viscosity and density. Measurements conducted with same Reynolds numbers instead of same volume flow rates gave in fact almost identical results.

The present results are in good agreement with the Boing and AAIB investigations that found a sticky range between $-5°C$ and $-20°C$, where ice crystals were most likely to adhere to their

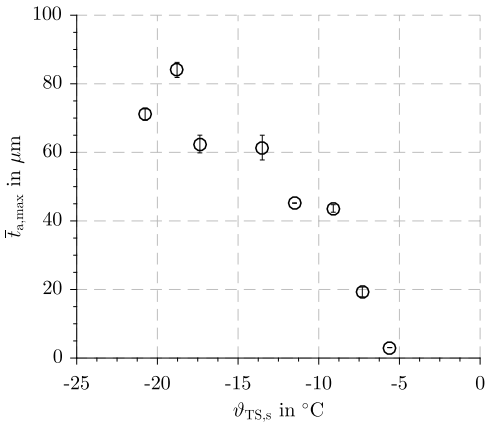

Fig. 8. Maximum average ice thickness $\bar{t}_{a,max}$ (Eq. (1)) on aluminium with glass bead blasted (GBB) surface finish in relation to the steady state test section fuel temperature $\vartheta_{TS,s}$ for $\dot{V}_t = 650$ l/h.

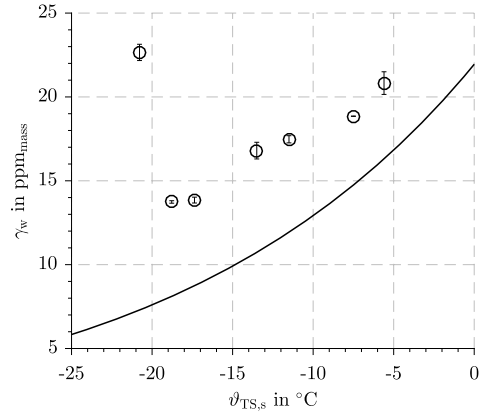

Fig. 9. Water content in Jet A-1 γ_w at the end of the cooling period (□ in Fig. 4) in relation to the steady state test section fuel temperature $\vartheta_{TS,s}$ for $\dot{V}_t = 650$ l/h. ○: total water content $\gamma_{w,t}$, —: measured water solubility $\gamma_{w,s}$.

surroundings [6]. In [12,4] such a sticky behaviour is described between $-12°C$ and $-18°C$.

The change in accretion behaviour below $-20°C$ seems to be a consequence of changing ice properties and might be linked to the ice adhesion strength. Archer et al. [19] measured the tensile interface strength of ice on aluminium substrates and observed a dramatic drop at a temperature of $-20°C$. They explained this by the thin liquid-like layer that is known to exist between ice and structural solids. Due to its damping effect, this layer would increase the stress required to separate the ice substrate interface. Between $-25°C$ and $-30°C$, the liquid layer and therefore the damping effect disappears. The interface strength approached an almost constant value. Similar relationships were also reported in [20] and [21].

In contrast to this, Dong et al. [22] measured an interface shear strength of ice on aluminium and copper plates that increased with decreasing temperature. Similar to Archer et al. [19], however, there was no further change with temperature below $-20°C$. Dong et al. also explained this by the liquid-like layer, but the gradually growing layer was believed to weaken the ice adhesion with increasing temperatures due to lubricating effects [22].

The role of a liquid like layer with regard to ice adhesion is not yet understood [23]. At higher temperatures there is a general agreement in the literature that the ice adhesion strength increases with temperature decrease [23]. This might be another contributing factor to the increasing ice thickness between $-6°C$ and $-15°C$ in Fig. 8, apart from a decreasing water solubility.

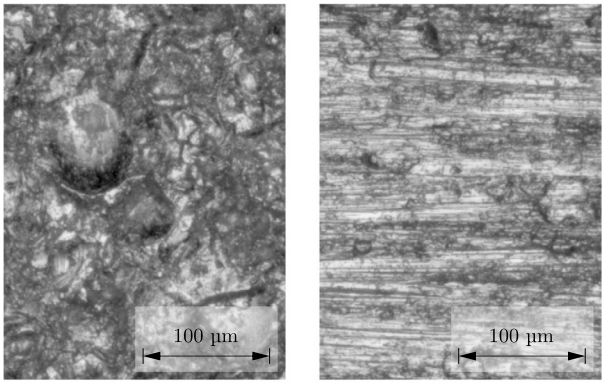

a) glass bead blasted (GBB) b) P400 abrasive paper (A400)

c) P3000 abrasive paper (A3000) d) mirror polished (POL)

Fig. 10. Micrographs showing the surface texture of the aluminium sample surfaces used to study the influence of surface topography.

Table 2
Arithmetic average roughness R_a of the aluminium (EN AW-AlMgSi) sample surfaces used to study the influence of surface topography.

name	method of processing	R_a in µm
GBB	glass bead blasted[1,2]	2.475 ± 0.149
A400	abrasive paper, P400	1.210 ± 0.020
A3000	abrasive paper, P3000	0.187 ± 0.003
POL	mirror polished	0.067 ± 0.003

[1] Reference surface treatment.
[2] Glass bead of 90–150 µm.

3.3. Influence of surface topography

Fig. 10 shows representative high magnification views of the test body surfaces used to study the effect of the surface topography. The corresponding roughness values R_a are given in Table 2. The roughest surface was obtained by glass bead blasting (GBB). The topography is characterised by large peaks and valleys ranging from approximately 10 µm–80 µm. The mirror polished surface (POL) has the lowest roughness. Here, only thin scratches are visible. The surfaces abraded with emery paper possess a roughness between these two. Both show similar characteristics, i.e. unidirectional grooves in the direction of abrasion. The grooves are smaller in size for the finer emery paper (A3000) than for the coarser one (A400).

In this section, the ice thickness results are normalized with the reference ice thickness according to

$$\overline{\Lambda}_{a,max} = \frac{\bar{t}_{a,max}}{\bar{t}_{a,max,ref}} \tag{3}$$

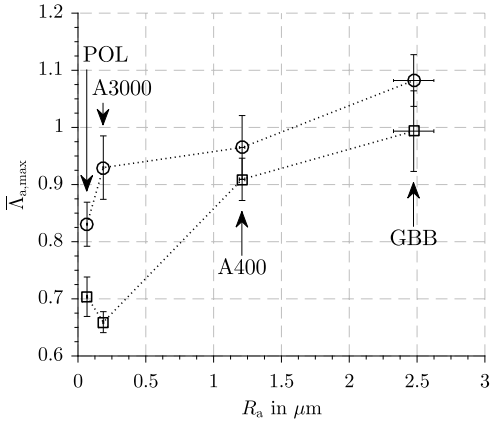

Fig. 11. Maximum average ice thickness ratio $\overline{\Lambda}_{a,max}$ (Eq. (3)) on aluminium in relation to the roughness R_a for $\vartheta_{TS,s} = -17.2°C$. ○: $\dot{V}_t = 220$ l/h, □: $\dot{V}_t = 650$ l/h.

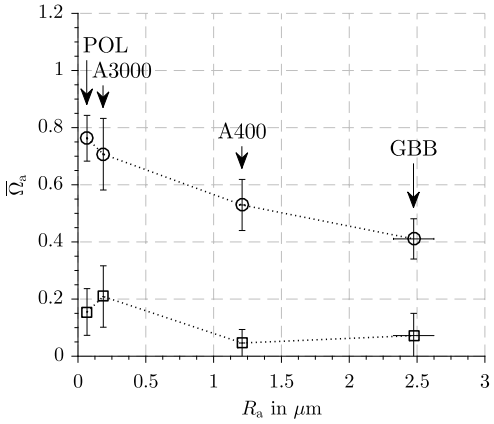

Fig. 12. Ice release ratio $\overline{\Omega}_a$ (Eq. (2)) on aluminium in relation to of the roughness R_a for $\vartheta_{TS,s} = -17.2°C$. ○: $\dot{V}_t = 220$ l/h, □: $\dot{V}_t = 650$ l/h.

where $\bar{t}_{a,max}$ is the maximum average ice thickness on the surface under investigation (upper half of the wedge) and $\bar{t}_{a,max,ref}$ is the maximum average ice thickness on the corresponding reference surfaces (lower half of the wedge), cf. Fig. 3. Since both measurements are obtained simultaneously during each run and therefore under same conditions, this direct comparison further reduces the influence of experimental uncertainties.

In Fig. 11 the maximum normalized ice thickness $\overline{\Lambda}_{a,max}$ is plotted against the surface roughness R_a. The dashed lines are drawn to guide the eye and do not mean that there is a linear relationship. Both volume flow rates show the same trend: the smoother the surface, the less the amount of ice. In case of the glass bead blasted surfaces (GBB) $\overline{\Lambda}_{a,max}$ is close to one. This is expected as the topography of this sample surface is identical to that of the also glass bead blasted reference surfaces. For the polished surface (POL), $\overline{\Lambda}_{a,max}$ drops to 0.704 (220 l/h) and 0.831 (650 l/h), respectively. The effect of surface roughness is more pronounced for the higher flow rate. This can be attributed to the higher shear forces acting on the (iced) test body surfaces. Higher shear or separating forces may enhance the significance of the effective counteracting ice-solid interface strength.

The release of ice due to the increasing volume flow rate (between □ and △ in Fig. 4) is illustrated in Fig. 12 in terms of the ice release ratio $\overline{\Omega}_a$. The figure shows that a higher fraction of ice is shed away from smoother surfaces. This means the ability of the already lower amounts of ice to withstand the increasing fluid dynamic forces deteriorates.

As for the temperature dependence, the correlation between ice thickness and surface roughness may be explained by the ice ad-

Table 3
Arithmetic average roughness R_a of the polished sample surfaces used to study the influence of material (wedge shaped test bodies, set 2).

name	material	R_a in µm
AL	aluminium alloy[1]	0.111 ± 0.004
SST	stainless steel[2]	0.017 ± 0.003
CU	copper[3]	0.137 ± 0.006
PMMA	polymethyl methacrylate	0.219 ± 0.012
PTFE	polytetrafluoroethylene	0.186 ± 0.007

[1] EN AW-AlMgSi [2] X5CrNi18-10 [3] Cu-ETP

hesion strength. Despite the very different methods employed in their studies, various authors found a significantly higher ice adhesion strength on mechanically roughened aluminium samples [19,20,24–26]. Zou et al. [24], Susoff et al. [25] and Wu et al. [20] explained this, in part, with the larger effective ice-solid contact area that is provided on rougher surfaces. In addition, according to [25,20,19], the larger peaks and valleys on rough surfaces contribute to the adhesion strength as they provide a greater likelihood for ice to mechanically interlock or actually anchor itself. It should be noted that in these studies the ice-solid interfaces were made from water samples or (supercooled) water droplets that froze directly onto the surfaces. Thus, the ice strength might have been also affected by the surface wettability or the number of nucleation sites for ice growth.

In this study, however, the ice layer is the result of impinging solid ice particles, as the above observations suggest (cf. Fig. 7). Nevertheless, some of the mechanisms described in literature can be carried over: The topology of the glass bead blasted (GBB) and coarsely abraded (A400) surfaces are characterised by large valleys and grooves that are similar in size compared to the ice particles entrained in the fuel. Hence, ice particles are in principle able to become trapped by the surface structures. This would increase their effective ice-solid contact area, might enable mechanical interlocking and, consequently, yield higher adhesion strength.

3.4. Influence of material

Three metals (Aluminium, AL; stainless steel, SST; copper, CU) and two plastics (PTFE; PMMA) were used to evaluate the influence of material. To reduce effects due to variations in surface roughness, a homogenous, smooth surface was created for all test surfaces by means of polishing. Table 3 shows the surface roughness R_a obtained for each material. Reflecting on the results with regard to the influence of surface roughness in Fig. 11, the remaining differences in roughness are believed to be too small to mask the material dependence.

Possible effects due to the different thermal properties are also negligible. Prior to the actual experiments, additional tests were carried out in order to evaluate the dynamic cooling behaviour of different test bodies, in particular the delay with which they follow the fuel temperature. For this, modified cylindrical test bodies ($d_C = 8$ mm) made of PMMA and aluminium were equipped with thermocouples to measure their core and surface temperatures. Additionally, a simulation model based on [27] was used to determine the dynamic temperature distribution within the material. Both, the experimental and simulation results showed that because of the moderate fuel cooling rate together with a high convective heat transfer between fuel and test body, the surfaces of all test bodies were able to follow the fuel temperature without significant delay, i.e. $\Delta\Theta < 0.1$ K. It therefore can be assumed that each of the test body surfaces had reached the steady state temperature before any ice accretion took place.

Fig. 13 presents the relationship between the maximum average ice thickness $\bar{t}_{a,max}$ and the different materials. For both volume flow rates, the ice thickness is much lower on plastics (PMMA, PTFE) in comparison to metals (AL, CU and SST). The average reduction is 49% (220 l/h) and 77% (650 l/h), respectively. Between the metals, no clear trend exists. Possible material effects seem to be small in regard to the experimental uncertainties. The same holds true with the two plastics.

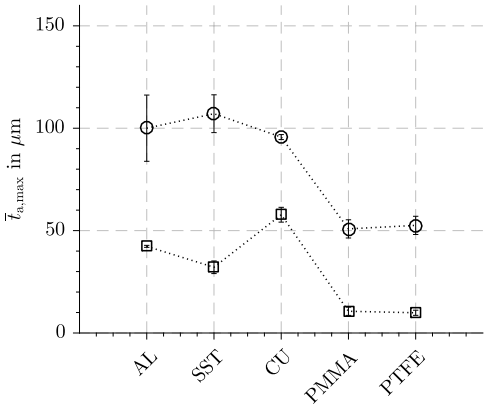

Fig. 13. Maximum average ice thickness $\bar{t}_{a,max}$ (Eq. (1)) on different materials with polished (POL) surface finish for $\vartheta_{TS,s} = -17.2$°C. ○: $\dot{V}_t = 220$ l/h, □: $\dot{V}_t = 650$ l/h.

The results on the release of ice are not shown in this paper as they reveal no clear relationship. This is a consequence of the very small amounts of ice involved especially in case of the plastics. Their detachment behaviour is subject to wide fluctuations and hence large measurement uncertainties.

The dramatic reduction in ice accretion in the case of PTFE seems to be the result of its so-called icephobic properties. PTFE is characterised by a very low surface energy. It has a very low affinity towards both water and ice [28]. Coatings of PTFE were found to reduce the ice adhesion strength by a factor of 5–7 with respect to the bare aluminium substrates [29,30,25]. In Menini et al. [31] the ice shear strength on aluminium substrates was reduced by a factor of almost 2.5 when coated with PTFE and Yang et al. [32] reported a shear strength for pristine (solid) PTFE plates that was 5% of that of bare aluminium.

For PMMA, the reports on the ice adhesion strength are less conclusive. In Archer et al. [19] the ice adhesion strength was reduced by a factor of 1.44 when bare aluminium substrates were coated with PMMA. They attributed this to the fewer number of bonding sites. Meuler et al. [33] found a reduction by as much as a factor of 1.51 with respect to untreated bare steel. Bharathidasan et al. [34], on the other hand, observed a 1.43 times higher ice adhesion for a PMMA coating on untreated aluminium. This, however, could also be explained by the fact that the PMMA surface possessed a significantly higher roughness.

Raraty et al. measured the ice adhesion strength on various metals. The results for brass and aluminium alloy were similar to those for stainless steel [35]. This is in agreement with the almost identical values for aluminium and stainless steel shown in [36]. Sonwalker et al. [37] reported the largest strength of ice on titanium, followed by copper, stainless steel, aluminium and PTFE. The differences between the metals, however, were small in comparison to PTFE.

With the exception of PMMA, all these observations correlate with the ice thickness found in this study.

4. Conclusions

A test rig was designed to mimic the icing conditions in flowing fuel. An optical measurement system was implemented to quantify ice formations down to a few micro metres in thickness. This allowed studying the icing process without any additional injection of water and hence with high reproducibility. A total number of

82 individual experiments were carried out in order to characterise the ice accretion and release process and to evaluate the effect of various key parameters. The main conclusions were as follows:

1. When the fuel was cooled below the saturation temperature, excess water was precipitated out in the form of fine water droplets having a diameter between 2 mm to 10 µm.
2. Ice accretion was most likely the result of impinging ice particles that had already transformed into their solidified crystalline form.
3. The ice particles behaved most “sticky” between temperatures ranging from about −6°C to −20°C.
4. The thickness of accreted ice increased with the degree of roughness for aluminium surfaces.
5. The thickness of accreted ice was similar between aluminium, copper and stainless steel; there was a significant reduction for PTFE and PMMA.
6. Collectively, the results showed a correlation between the amount of accreted ice and the general trends in ice adhesion strength described in literature.

The findings regarding the tendency to icing are believed to be of general validity and may serve as guidance for an icephobic aircraft fuel system design in which ice minimally adheres.

Conflict of interest statement

We wish to confirm that there are no known conflicts of interest associated with this publication and there has been no significant financial support for this work that could have influenced its outcome.

We confirm that the manuscript has been read and approved by all named authors and that there are no other persons who satisfied the criteria for authorship but are not listed. We further confirm that the order of authors listed in the manuscript has been approved by all of us.

We confirm that we have given due consideration to the protection of intellectual property associated with this work and that there are no impediments to publication, including the timing of publication, with respect to intellectual property. In so doing we confirm that we have followed the regulations of our institutions concerning intellectual property.

We understand that the Corresponding Author is the sole contact for the Editorial process (including Editorial Manager and direct communications with the office). He/she is responsible for communicating with the other authors about progress, submissions of revisions and final approval of proofs. We confirm that we have provided a current, correct email address which is accessible by the Corresponding Author and which has been configured to accept email from mathias.schmitz@tuhh.de.

Acknowledgements

The research leading to these results has received funding from the European Union Seventh Framework Programme (FP7/2007-2013) under grant agreement no. 314032.

References

[1] CRC, Handbook of Aviation Fuel Properties, Tech. rep., Coordinating Research Council, Inc., Alpharetta, 2004.
[2] J.K.-W. Lam, M.D. Carpenter, C.A. Williams, J.I. Hetherington, Water solubility characteristics of current aviation jet fuels, Fuel 133 (2014) 26–33, https://doi.org/10.1016/j.fuel.2014.04.091.
[3] V.L. Zherebtsov, M.M. Peganova, Water solubility versus temperature in jet aviation fuel, Fuel 102 (2012) 831–834, https://doi.org/10.1016/j.fuel.2012.06.070.
[4] SAE, AIR790C: Considerations on Ice Formation in Aircraft Fuel Systems, Tech. rep., Society of Automotive Engineers International: Ae-5a Aerospace Fuel, Inerting and Lubrication Sys Committee, Aug. 2006.
[5] S. Baena-Zambrana, S.L. Repetto, C.P. Lawson, J.K.-W. Lam, Behaviour of water in jet fuel – a literature review, Prog. Aerosp. Sci. 60 (2013) 35–44, https://doi.org/10.1016/j.paerosci.2012.12.001.
[6] AAIB, Report on the Accident to Boeing 777-236ER, G-YMMM, at London Heathrow Airport on 17 January 2008, Tech. rep., Air Accidents Investigation Branch, Department for Transport (UK), Hampshire, 2010.
[7] B.J. Murray, S.L. Broadley, G.J. Morris, Supercooling of water droplets in jet aviation fuel, Fuel 90 (2011) 433–435, https://doi.org/10.1016/j.fuel.2010.08.018.
[8] J.K.-W. Lam, J.I. Hetherington, M.D. Carpenter, Ice growth in aviation jet fuel, Fuel 113 (2013) 402–406, https://doi.org/10.1016/j.fuel.2013.05.048.
[9] L. Lao, C. Ramshaw, H. Yeung, M. Carpenter, J. Hetherington, J.K.-W. Lam, S. Barley, Behaviour of water in jet fuel in a simulated fuel tank, Society of Automotive Engineers 2011–01–2794, https://doi.org/10.4271/2011-01-2794.
[10] Y. Hayashi, A. Aoki, S. Adachi, K. Hori, Study of frost properties correlating with frost formation types, J. Heat Transf. 99 (1977) 239–245, https://doi.org/10.1115/1.3450675.
[11] J.K.-W. Lam, L. Lao, D.W. Hammond, J.P. Power, Character and interface shear strength of accreted ice on subcooled surfaces submerged in fuel, Aeronaut. J. 119 (1221) (2015) 1377–1396, https://doi.org/10.1017/s0001924000011301.
[12] SAE, ARP1401B: Aircraft Fuel System and Component Icing Test, Tech. rep., Society of Automotive Engineers International: Ae-5a Aerospace Fuel, Inerting And Lubrication Sys Committee, Jun. 2012.
[13] E. Marechal, S. Khelladi, F. Ravelet, F. Bakir, Towards numerical simulation of snow showers in jet-engine fuel systems, in: SimHydro 2014: Modelling of rapid transitory flows, 2014.
[14] J. Schindelin, I. Arganda-Carreras, E. Frise, V. Kaynig, M. Longair, T. Pietzsch, S. Preibisch, C. Rueden, S. Saalfeld, B. Schmid, J.-Y. Tinevez, D.J. White, V. Hartenstein, K. Eliceiri, P. Tomancak, A. Cardona, Fiji: an open-source platform for biological-image analysis, Nat. Methods 9 (7) (2012) 676–682, https://doi.org/10.1038/nmeth.2019.
[15] S. Baena, J.K.-W. Lam, C. Lawson, Effects of ice accretion in an aircraft protective mesh strainer of a fuel pump, in: SAE Technical Paper Series, SAE International, 2015.
[16] WAFCOLT, Water Behaviour in Aviation Fuel Under Cold Temperature Conditions, Final report, European Aviation Safety Agency, Mar. 2013.
[17] R. Hill, W.J. Hughes, A Review of the Flammability Hazard of Jet a Fuel Vapor in Civil Transport Aircraft Fuel Tanks, Tech. rep., Federal Aviation Administration, Jun. 1998.
[18] J.C. for Guides in Metrology, Evaluation of Measurement Data – Guide to the Expression of Uncertainty in Measurement, Tech. rep., Bureau International des Poids et Mesures, 2008.
[19] P. Archer, V. Gupta, Measurement and control of ice adhesion to aluminum 6061 alloy, J. Mech. Phys. Solids 46 (10) (1998) 1745–1771, https://doi.org/10.1016/s0022-5096(98)00014-3.
[20] R.-R. Wu, C.-L. Zhu, C.-X. Zhu, B. Miao, Adhesive mechanism and experimental study on shear adhesive strength of impact ice, Adv. Mater. Res. 937 (2014) 330–335, https://doi.org/10.4028/www.scientific.net/amr.937.330.
[21] O. Nickolayev, V. Petrenko, SFM studies of the surface morphology of ICE, MRS Proc. 355 (1994), https://doi.org/10.1557/proc-355-221.
[22] W. Dong, J. Ding, Z.X. Zhou, Experimental study on the ice freezing adhesive characteristics of metal surfaces, J. Aircr. 51 (3) (2014) 719–726, https://doi.org/10.2514/1.c032393.
[23] A. Work, Y. Lian, A critical review of the measurement of ice adhesion to solid substrates, Prog. Aerosp. Sci. 98 (April 2018) 1–26, https://doi.org/10.1016/j.paerosci.2018.03.001.
[24] M. Zou, S. Beckford, R. Wei, C. Ellis, G. Hatton, M. Miller, Effects of surface roughness and energy on ice adhesion strength, Appl. Surf. Sci. 257 (8) (2011) 3786–3792, https://doi.org/10.1016/j.apsusc.2010.11.149.
[25] M. Susoff, K. Siegmann, C. Pfaffenroth, M. Hirayama, Evaluation of icephobic coatings – screening of different coatings and influence of roughness, Appl. Surf. Sci. 282 (2013) 870–879, https://doi.org/10.1016/j.apsusc.2013.06.073.
[26] H.H.G. Jellinek, Adhesive properties of Ice, Part 2, report 62, US Army Snow Ice & Permafrost Research Establishment, 1960.
[27] H.D. Baehr, K. Stephan, Heat and Mass Transfer, Springer, 2006.
[28] R. Karmouch, S. Coude, G. Abel, G.G. Ross, Icephobic PTFE coatings for wind turbines operating in cold climate conditions, in: 2009 IEEE Electrical Power & Energy Conference (EPEC), 2009.
[29] C. Laforte, A. Beisswenger, Icephobic material centrifuge adhesion test, in: Proceedings of IWAIS, Montreal, Canada, 2005.
[30] G. Fortin, A. Beisswenger, J. Perron, Centrifuge adhesion test to evaluate icephobic coatings, in: AIAA Atmospheric and Space Environments Conference, American Institute of Aeronautics and Astronautics, 2010.
[31] R. Menini, M. Farzaneh, Elaboration of Al2O3/PTFE icephobic coatings for protecting aluminum surfaces, Surf. Coat. Technol. 203 (14) (2009) 1941–1946, https://doi.org/10.1016/j.surfcoat.2009.01.030.
[32] S. Yang, Q. Xia, L. Zhu, J. Xue, Q. Wang, Q. Chen, Research on the icephobic properties of fluoropolymer-based materials, Appl. Surf. Sci. 257 (11) (2011) 4956–4962, https://doi.org/10.1016/j.apsusc.2011.01.003.

[33] A.J. Meuler, J.D. Smith, K.K. Varanasi, J.M. Mabry, G.H. McKinley, R.E. Cohen, Relationships between water wettability and ice adhesion, ACS Appl. Mater. Interfaces 2 (11) (2010) 3100–3110, https://doi.org/10.1021/am1006035.
[34] T. Bharathidasan, S.V. Kumar, M.S. Bobji, R.P.S. Chakradhar, J.B. Bharathibai, Effect of wettability and surface roughness on ice-adhesion strength of hydrophilic, hydrophobic and superhydrophobic surfaces, Appl. Surf. Sci. 314 (2014) 241–250, https://doi.org/10.1016/j.apsusc.2014.06.101.
[35] P.V. Hobbs, Ice Physics, Oxford University Press, Oxford, 2010.
[36] R.J. Scavuzzo, M.L. Chu, Structural Properties of Impact Ices Accreted on Aircraft Structures, Tech. rep., The University of Akron, Mechanical Engineering Department – NASA Lewis Research Center, Jan. 1987.
[37] N. Sonwalkar, S.S. Sunder, S.K. Sharma, Ice/solid adhesion analysis using low-temperature raman microprobe shear apparatus, Appl. Spectrosc. 47 (10) (1993) 1585–1593, https://doi.org/10.1366/0003702934334606.